ADVANCED MATERIALS INTERFACES
Open Access
www.advmatinterfaces.de

Adsorbate Formation/Removal and Plasma-Induced Evolution of Defects in Graphitic Materials

*Anna L. Eichhorn, Marvin Hoffer, Katharina Bitsch, and Christian Dietz**

The preparation of adsorbate-free graphene with well-defined layer numbers is a current challenge in materials and surface science and required to fabricate graphene-based nanodevices, such as used in nanoelectromechanical systems. One strategy to tailor the layer number is oxygen-plasma treatment of few-layer graphene/graphite flakes. However, when graphitic materials are stored in air under ambient conditions, it is almost inevitable that adsorbates deposit on their surfaces. When precisely removing individual graphene layers from graphitic flakes by oxygen-plasma treatment, the amount and type of adsorbates strongly affect the required plasma-treatment process and duration. To examine the removal/etching mechanism involved in removing such layers, few-layer graphene/graphite flakes, with areas of different layer numbers, are stored in ambient air and stepwise exposed to oxygen plasma in a shielded configuration. The flakes are then successively analyzed by multifrequency atomic force microscopy together with Raman spectroscopy, focusing on etching rate, and adsorbate and defect evolution. Combined in-plane and out-of-plane tip–adsorbate–substrate interaction analysis facilitates discrimination of different types of adsorbates (water, polycyclic aromatic hydrocarbons, and linear alkanes) and their formation with time. The results demonstrate the potential regarding the development of an efficient method for cleaning of graphitic surfaces and ablation of individual graphene layers.

1. Introduction

Since its invention in 2004,[1] graphene has emerged as a promising material as electrical component in storage and energy conversion devices, such as batteries[2] and solar cells,[3] paving the way toward alternative energy sources.[4,5] Depending on the application, graphene with a specific number of layers is required, and mono-, bi-, and trilayer graphene are of particular technological interest.[6–8] Raman spectroscopy has been shown to be a reliable method for optical characterization of graphite and graphene. Four characteristic peaks, i.e., G-, D-, 2D-, and D'-peak can be analyzed in the Raman spectrum of graphitic materials. If spectra are acquired with a laser wavelength of 532 nm, these peaks are located at ≈1580, 1320, 2700, and 1620 cm^{-1}. The G-peak originates from the excitation of the two-dimensional E_{2g} phonon mode [9] and the D-peak represents the activation of the A_{1g} phonon mode that is caused by defects in graphitic materials.[10] The overtone of the D-peak is the 2D-peak where two in-plane transverse optical phonon modes are excited.[11] The D'-peak stems from the scattering processes at small momentum phonons in defective graphite and graphene.[12] The intensity ratio between the G- and the 2D-peak can provide information about the sample thickness.[13] Despite several graphene preparation methods being realized within the last few years,[1,14–17] the synthesis of graphene with a well-defined number of layers is still challenging. A promising approach for the controlled ablation of graphene layers is plasma treatment. Several different gases have been used for thinning multilayer graphene to monolayer graphene, such as nitrogen (N_2), hydrogen (H_2), hydrogen peroxide (H_2O_2), and oxygen (O_2), or combinations of these gases.[18–21] The time required for the ablation of single layers is strongly dependent on the type of gas used [20] and on ablation parameters, such as the discharge power, plasma chamber pressure, and distance of the sample from the powered electrode.[22–24] Oxygen plasma is strongly effective in graphene layer ablation; however, the ablation parameters must be carefully adjusted in order to prevent the sample from becoming severely damaged. Eckmann et al.[25] analyzed the Raman spectra of defective graphene samples regarding the intensity ratios of the D-, G-, and D'-peaks. By inspecting the intensity of the D'-peak which represents the strength of the peak induced by the defects of the graphene samples, they derived that the intensity ratio between the D- and the D'-peak is a suitable indicator of the predominant type of defect. The authors found that $I_D/I_{D'} \approx 13$ indicated that sp^3-type defects were predominant, while $I_D/I_{D'} \approx 7$ indicated that vacancy-like defects

A. L. Eichhorn, M. Hoffer, K. Bitsch, C. Dietz
Physics of Surfaces
Institute of Materials Science
Technische Universität Darmstadt
Peter-Grünberg-Str. 2, 64287 Darmstadt, Germany
E-mail: dietz@pos.tu-darmstadt.de

The ORCID identification number(s) for the author(s) of this article can be found under https://doi.org/10.1002/admi.202300256

DOI: 10.1002/admi.202300256

were predominant. Smaller intensity ratios between the D- and the D'-peak (≈3.5) were attributed to boundaries in the graphite. Lee et al.[26] defined different stages of defect generation based on the aforementioned intensity ratio between D- and D'-peak. They deduced that the transition between sp^3- (stage 1, crystalline defects) and vacancy-type defects (stage 2, nanocrystalline defects) occurred at $I_D/I_{D'} \approx 7$. The third stage of defect generation was defined by reaching a plateau at $I_D/I_{D'} \approx 3.5$, indicating the presence of amorphous carbon.[27] Zandiatashbar et al.[28] reported that the introduction of defects in graphene samples during plasma treatment could be strongly reduced by placing the sample upside down in the chamber on two glass slides, resulting in a shielded configuration. An illustration of the shielded configuration was shown by Lee et al.[26] Additionally, they found that the ratio between the D- and G-peak as a function of plasma-treatment time of monolayer graphene had a local maximum at the transition between predominantly sp^3-type and predominantly vacancy-type defects.[28] Because the number of defects and the number of layers both influence the Raman spectra of few-layer graphene/graphite samples, we examined the effect of plasma treatment on the few-layer graphene/graphite samples during stepwise ablation of the graphene layers. This was done in a shielded configuration, and the samples were interrogated using Raman spectroscopy and atomic force microscopy (AFM). These both techniques were used in this study for the identification of the adsorbate species on µm-sized, substrate-supported few-layer graphene/graphite flakes because conventional methods for adsorbate analysis, e.g., X-ray photoelectron spectroscopy (XPS) exhibit major issues, such as detection limits caused by the X-ray beam diameter, hydrogen atoms, and desorption of adsorbates from the sample surface in ultra-high vacuum during analysis. A detailed study about XPS on highly oriented pyrolytic graphite (HOPG) has been conducted by Pálinkás et al.[39] Graphene samples have a high tendency to become covered by adsorbates, which, depending on the duration of storage and surrounding conditions, form stripe-like structures with periodicities of 4–6 nm.[29–39] Recently, we demonstrated (using AFM) that different types of adsorbates covering graphitic surfaces could be distinguished with high resolution by analyzing the flexural and torsional/lateral cantilever vibrational modes simultaneously (AMFlex2-OLTor1-FMLat1-FMFlex3 mode), when the tip interacted with the adsorbates.[36] Pronounced contrasts were visible in the flexural phase and lateral drive amplitude of the AFM measurements. These observables provide valuable information about the dissipative tip–adsorbate interactions. The origin of the contrasts can be explained based on the adsorbates as soft species dissipating more energy by the interaction with the AFM tip compared to the dissipation of the tip with underlying graphitic surfaces as crystalline material. Besides the stripe-like patterns identified by Pálinkás et al.,[39] which originated from normal alkanes with chain lengths between 20 and 26 carbon atoms, we found another four types of adsorbates that could be attributed to three different polycyclic aromatic hydrocarbons (PAHs) and water.[40] Consequently, when removing individual carbon layers from graphitic surfaces, it is essential to remove adsorbates at an earlier stage.

We also examined the controlled removal of adsorbates by shielded oxygen-plasma treatment in order to obtain cleaned and pure graphitic surfaces. The effect of incremental oxygen-plasma treatment on a few-layer graphene/graphite sample stored for different durations under ambient laboratory conditions was analyzed by using AFM, with the recently introduced AMFlex2-OLTor1-FMLat1 AFM method.[41] This multifrequency approach was chosen because of its capability of distinguishing different types of adsorbates by their in-plane and out-of-plane interactions with the AFM tip. Additionally, this approach facilitated the examination of whether surfaces were covered with adsorbates.[40]

2. Results and Discussion

2.1. Layer Analysis of Oxygen-Plasma-Treated Few-Layer Graphene/Graphite Flakes

To elucidate the effect of oxygen-plasma treatment on layer number and defect generation within a few-layer graphene/graphite sample, AFM, and Raman spectroscopy experiments were performed. The sample was placed in a plasma chamber in a shielded configuration, as schematically depicted in **Figure 1**b. After each step of oxygen-plasma treatment, the sample was analyzed using amplitude modulation (AM) AFM and Raman spectroscopy; scans across the different layers of a graphene flake were acquired. The sample was oxygen-plasma-treated for the durations listed in **Table 1** of the Experimental Section.

Figure 1 shows the evolution of layer thickness for a few-layer graphene/graphite sample stepwise treated by oxygen plasma in a shielded configuration, as schematically depicted in Figure S1 (Supporting Information). In Figure 1a, AFM topographic images of a few-layer graphene/graphite sample are shown prior to and after different durations of plasma treatment. The corresponding cross-sections along the white line in Figure 1a (blue framed image) are shown in Figure 1b. Additionally, areas A, B, C, and D, representing graphene/graphite with different layer thicknesses, are marked in Figure 1a (blue frame and yellow markings) and in Figure 1b. These areas were selected according to signficant height differences in form of plateaus visible in the cross-sections of Figure 1b to simplify the analysis of the influence of oxygen plasma on the layer number of the few-layer graphene/graphite flake. Surprisingly, the height of the few-layer graphene/graphite sample determined from the cross-section of the AFM images of the sample prior to oxygen-plasma treatment (light blue frame) is less than the height determined after 2.5 min (gray frame) of oxygen-plasma treatment. This appears confusing because it would imply a faster removal of silicon dioxide (SiO_2) compared with graphitic material. However, if the corresponding topographic images in Figure 1a (light blue and gray framed) are analyzed in detail, it becomes obvious that prior to plasma treatment, the substrate was covered significantly by adsorbates (left and right portions of the cross-section (light blue curve in Figure 1b)). This phenomenon was also observed and analyzed in detail in our recent publication,[40] in which we showed that different types of adsorbates formed on both, graphene/graphite sample and Si/SiO_2-substrate. Consequently, it is reasonable to assume that a larger quantity of adsorbates covered the Si/SiO_2-substrate area compared to the graphene/graphite sample, resulting in an apparently smaller thickness of the graphene/graphite sample prior to plasma treatment. A detailed discussion of this assumption is provided in Figure S8 (Supporting Information). Furthermore, by analyzing cross-sections of AFM topographic images taken after 30 s, 1 min, 1.5 min, and 2 min, shown in

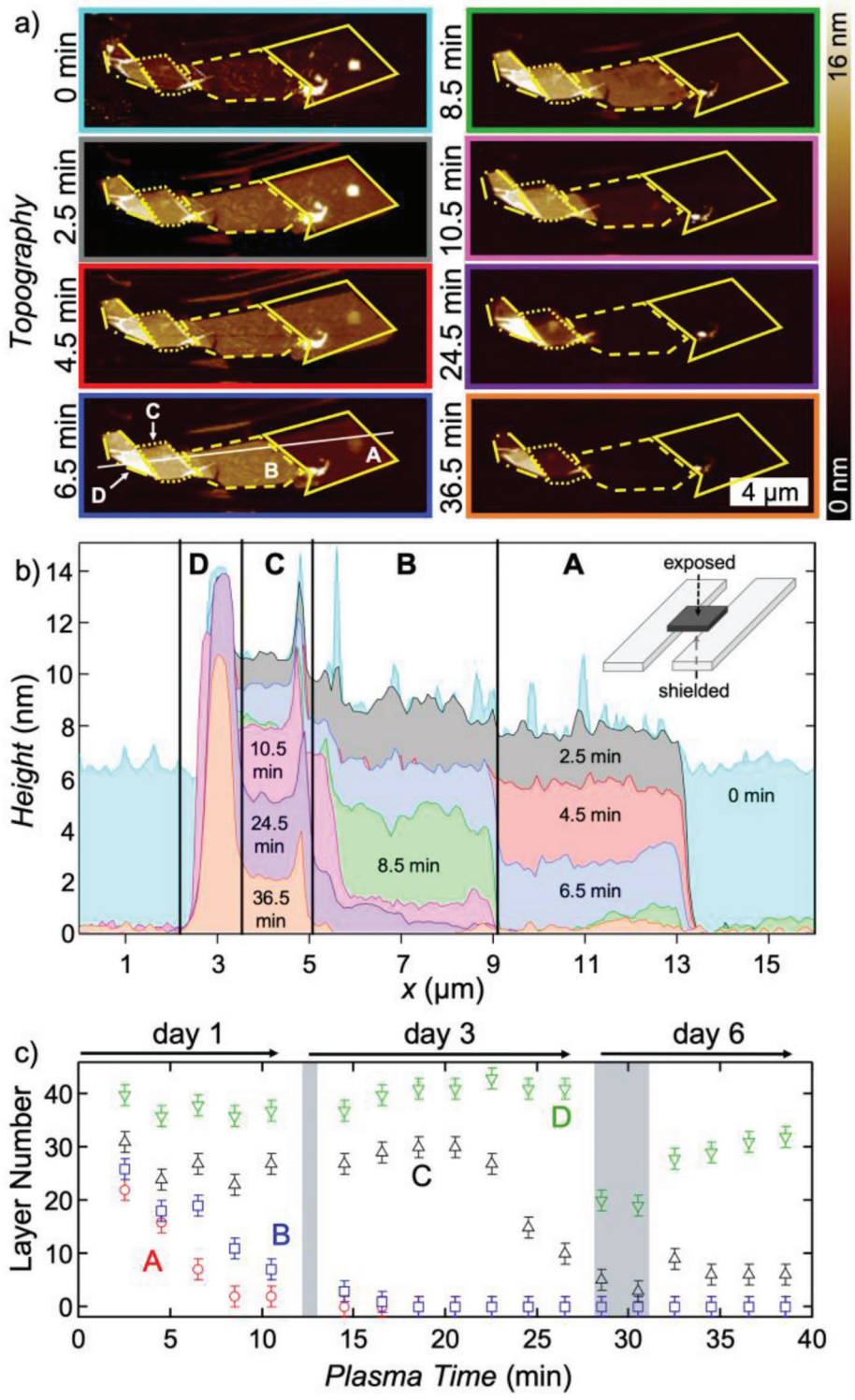

Figure 1. AFM topography imaging and analysis of a few-layer graphene/graphite sample treated by oxygen plasma. a) AFM topography images and b) cross-sections of a few-layer graphene/graphite flake before (light blue) and after 2.5 min (gray), 4.5 min (red), 6.5 min (blue), 8.5 min (green), 10.5 min (pink), 24.5 min (purple), and 36.5 min (orange) of oxygen-plasma treatment in a shielded configuration (inset in (b)). c) Number of carbon layers of the different areas A (red circle), B (blue square), C (black triangle), and D (green triangle), as marked in (b), as a function of plasma-treatment time. Error bars include the standard deviation resulting from cross-sectional profiles as well as uncertainties of height measurements due to possible adsorbates present (±2 layers). The time labels on top of the graph in (c) represent the time after preparation of the few-layer graphene/graphite flake. The Raman and AFM measurements depicted in this figure were not conducted within a single day owing to the time-intensive nature of layer analysis, which presents a potential source of error.

Figure S2 (Supporting Information), we can show that the fluctuations in height on the Si/SiO_2-substrate (very left and right portions) within the cross-sections get less distinct with increasing plasma-treatment time. This indicates that a higher quantity of adsorbates is removed with increasing plasma time. After 2.5 min of plasma treatment, the Si/SiO_2-substrate area seems to be cleaned from adsorbates. In order to reduce adsorbate induced errors in the calculation of layer numbers from height-profiles, the first values were determined after 2.5 min of plasma-treatment as shown in Figure 1c. Nevertheless, it needs to be mentioned that the calculation of layer numbers from AFM topography images taken under ambient conditions needs to be interpreted with care due to the possibility that adsorbates might still cover portions of the few-layer graphene/graphite flake. For example after 4.5 min of plasma treatment, no significant height difference between area A and B can be seen, however, after 6.5 min of plasma treatment. This could mean that the sample was cleaned after 4.5 min, removing a large quantity of adsorbates, and at 6.5 min the actual ablation of graphene layers started. Interestingly, the etching rate of graphene layers was strongly dependent on the initial number of layers, as can be deduced from Figure 1c. As also shown by Xie et al.,[42] the larger the initial number of graphene layers, the slower the etching rate. We assume that this is because of the presence of different types of adsorbates on the substrate/sample, and the associated differences in adsorption energies. The removal of the thinner graphene layers (areas A and B) started immediately after the adsorbates were removed, whereas 24.5 min elapsed before a clear reduction in thickness was visible in area C and after 32.5 min in area D. Interestingly, there was a continuous removal of material within areas A and B until exposure of the substrate after 8.5 and 12.5 min, respectively. The etching rates within areas A (2.5–8.5 min), B (6.5–12.5 min), and C (24.5–28.5 min) were 3.0–3.5 layers per min, i.e., 16–21 s were required to remove a single layer of graphene. However, these ascertained rates are not easy to transfer to other plasma treatment processes. In the actual application scenario there are several parameters that can affect the graphene layer ablation and defect generation. The gas type is crucial whether and what type of functional groups are formed at the graphene flake surface. The plasma treatment time, discharge power, distance from the powered electrode, and configuration, meaning direct or shielded exposure, have to be considered as well.

2.2. Defect Analysis of Oxygen-Plasma-Treated Few-Layer Graphene/Graphite Flakes

To study the effect of stepwise oxygen-plasma treatment on defect evolution in the few-layer graphene/graphite sample, we took Raman measurements after each step of plasma treatment, immediately after the AFM topographic images (cf. Section 2.1) were taken. The results are summarized in **Figure 2**.

The AFM topographic image taken after 6.5 min of plasma treatment is shown in Figure 2a and indicates areas A, B, C, and D, where the Raman spectra were taken. Results of the Raman-spectroscopic analysis are shown in Figure 2b in the form of the intensity ratios D/G (red, measure for defect density), 2D/G (blue, measure for layer number), and D/D' (purple, measure for defect type) determined within the areas A (circle), B (square), C (triangle pointing up), and D (triangle pointing down). Additionally, a zoom-in for the first 2 min of cumulative oxygen-plasma treatment is provided in Figure 2c,d for the intensity ratios D/G and 2D/G, respectively. For comparison, the results of a HOPG sample, stepwise treated for 120 s, are included in Figure 2c,d (filled hexagons).

Each of the areas A, B, C, and D show an initial increase in the intensity ratio D/G. Interestingly, for areas A and B a maximum in the intensity ratio between the D- and G-peaks at ≈3 was reached shortly before the area was completely removed as a consequence of oxygen-plasma treatment. Such a maximum was also observed by Zandiatashbar et al.[28] at $I_D/I_G \approx 4$, which was interpreted as a transition between predominantly sp^3-type and vacancy-type defects. However, the authors observed a complementary decrease in $I_D/I_{D'}$, which was not observed in our experiments. This may be because Zandiatashbar et al.[28] investigated monolayer graphene, whereas we focused on controlled ablation of few-layer graphene/graphite samples. In contrast, for the intensity ratio D/D' (Figure 2b, purple) no clear trend was observable. For areas A and B, I_D/I_D' was stable at ≈6.4 ± 0.5 and 5.5 ± 0.4, respectively; there was slightly more variance for areas C and D (3.6 ± 1 and 3.7 ± 0.8). Based on the experiments done by Eckmann et al.[25] on graphene, the predominant types of defects would be the vacancy-type (≈7) in areas A and B and the boundary-type (≈3.5) in areas C and D. However, this is in contrast to the interpretation by Zandiatashbar et al.[28] that at $I_D/I_{D'} < 7$ a vacancy-type of defects is to be expected as it was the case for the areas C and D in the presented work. This contradiction shows how controversial the literature regarding the different defect stages of plasma treated graphitic materials is. It is important to consider that not only the number of defects, but also the number of layers influences the Raman spectra.[43] This argument is supported by the trend of the intensity ratio I_{2D}/I_G (Figure 2b,d, blue), which was initially larger for thinner areas of the flake, but decreased with plasma-treatment time. Lee et al.[26] found that during stage 1 (prior to reaching the maximum value of I_D/I_G) oxygen tended to adsorb on the graphene surface to form sp^3-type defects, such as epoxy, carbonyl, and ether groups. The epoxy groups exhibited, according to the authors, the lowest defect formation energy and were energetically favored to form on the graphene surface. The transition between

Table 1. Oxygen-plasma times for treatment of the few-layer graphene/graphite flake as analyzed in Figures 1 and 2.

	Step 1	Step 2	Steps 3–6	Steps 7–25
Treatment time	10 s	20 s	30 s	2 min
Cumulative treatment time	10 s	30 s	1 min, 1.5 min, 2 min, 2.5 min	4.5 min, 6.5 min, 8.5 min, 10.5 min, 12.5 min, 14.5 min, 16.5 min, 18.5 min, 20.5 min, 22.5 min, 24.5 min, 26.5 min, 28.5 min, 30.5 min, 32.5 min, 34.5 min, 36.5 min, 38.5 min, 40.5 min

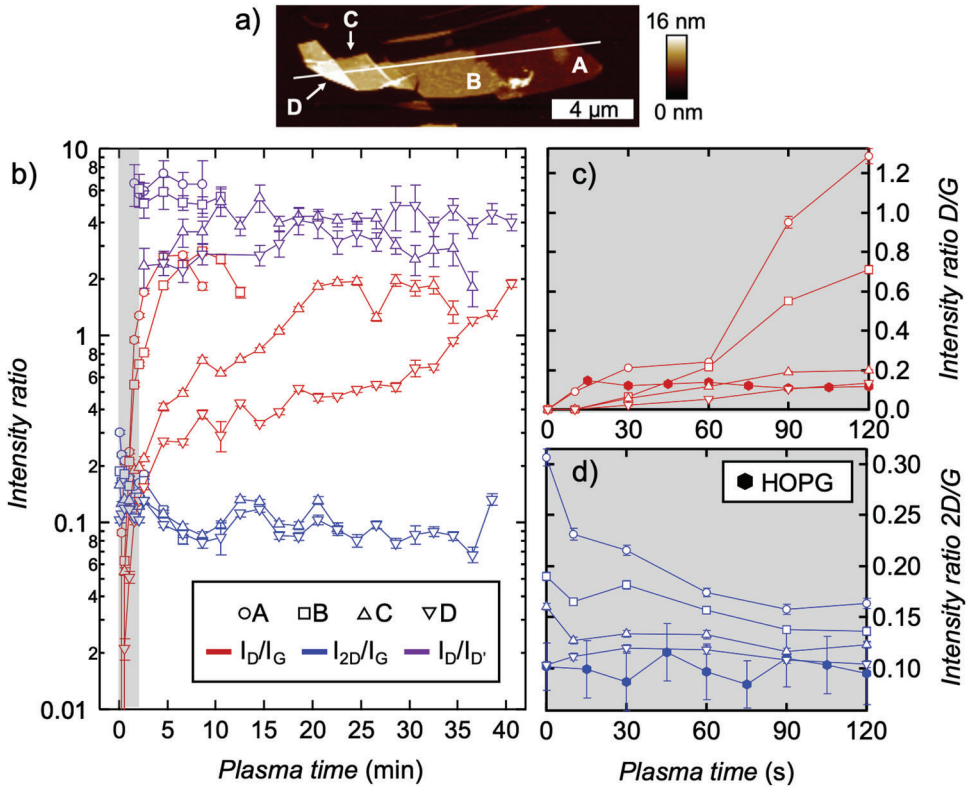

Figure 2. a) Raman intensity ratios measured within areas A (circle), B (square), C (triangle pointing up), and D (triangle pointing down), as marked in (a), b) as a function of oxygen-plasma treatment time. The intensity ratio between the D- and G-peak is shown as a function of plasma-treatment time in red, between the 2D- and G-peak in blue and between the D- and D'-peak in purple color. Zoom-in images of the gray marked area in (b) for the intensity ratios c) D/G and d) 2D/G. For comparison, the intensity ratios determined on HOPG for stepwise oxygen-plasma treatment in the shielded configuration are added to (c) and (d) by means of filled hexagons. Error bars represent the uncertainties occurring by fitting the peaks in the recorded Raman spectra.

stage 1 and 2 represented the conversion of sp^3- to vacancy-type defects.

Additionally, we observed that the D-peak already appeared after 30 s of oxygen-plasma treatment at the latest for all areas of the investigated few-layer graphene/graphite flake including the HOPG sample (see Figure 2c). This was unexpected because, for short plasma-treatment times, the graphene/graphite flakes were still covered by large quantities of adsorbates (Figure 1). Consequently, we decided to analyze the process of adsorbate removal by successive oxygen-plasma treatment in more detail by applying the recently introduced AMFlex2-OLTor1-FMLat1 AFM method. This method allows a detailed analysis of the in-plane and out-of-plane interactions of a sharp tip with adsorbates and graphitic surfaces.[41] Based on the findings of Zandiatashbar et al.[28] and Lee et al.,[26] we propose that for 30 s of plasma treatment predominantly sp^3-type defects, such as epoxy, carbonyl, and ether groups, should be visible. Depending on the thickness of the few-layer graphene/graphite sample, longer plasma-treatment durations should either lead to the formation of further sp^3-type defects or to vacancies whose presence we also aimed to confirm by the multifrequency AFM method.

2.3. Domain Pattern Formation and Successive Removal by Oxygen Plasma

In our previous work[40] we observed water islands and PAH domains as we analyzed a few-layer graphene/graphite flake surface 4 h after sample preparation and after 14 days of sample storage alkanes were visible in form of stripe-like patterns. Therefore, we expected these adsorbate structures on the surface to become evident upon storage. Firstly, we analyzed the second flexural phase and lateral drive amplitude AFM images acquired on a stored and oxygen-plasma-treated few-layer graphene/graphite flake at a relatively large scale (8 × 8 μm^2). The results are shown in **Figure 3**.

For the images shown in Figure 3, the sample was first stored for two weeks (Figure 3a,h), then for another three weeks (Figure 3b,i), and then treated with oxygen-plasma for 30 s in the shielded configuration (Figure 3c,j). Subsequently, we repeated a procedure of one week's storage (Figure 3d,f,k,m and Figure S4a,c, Supporting Information) and 30 s of plasma treatment (Figure 3e,g,l,n and Figure S4b,d, Supporting Information) three times, to study the desorption and re-adsorption process of adsorbates.

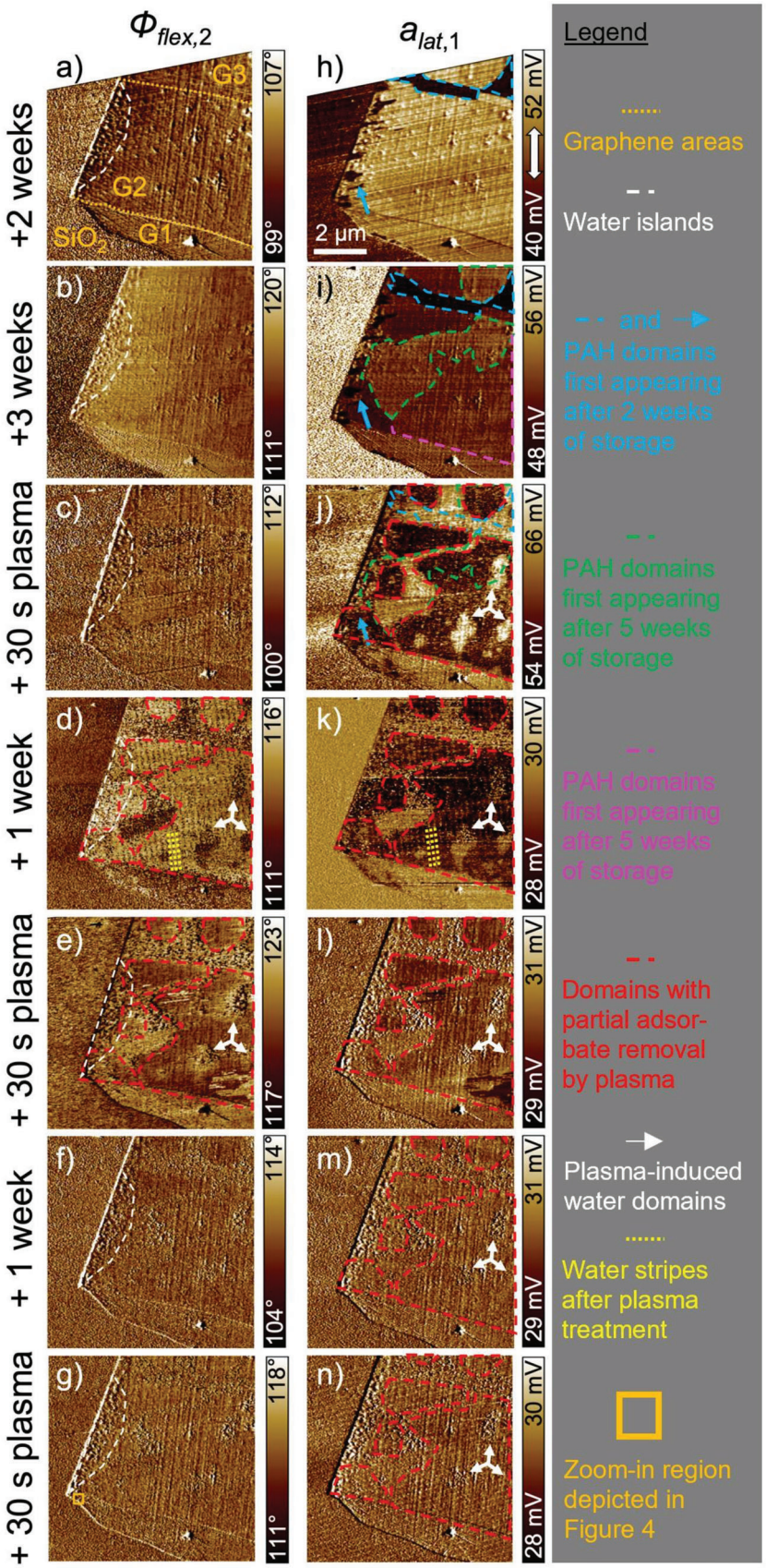

After the initial storage of the prepared graphene/graphite sample for two weeks, the accumulation of adsorbates on the few-layer graphene/graphite flake was characterized by different domains apparent, as highlighted by the blue arrow and dashed lines in the lateral drive amplitude image in Figure 3h. Interestingly, the domains were not visible in the corresponding second flexural phase image (Figure 3a). However, the flexural phase image indicated the presence of adsorbates forming large-scale islands within the area marked by the white dashed line in Figure 3a. These islands were also observed in our recent study,[40] and most likely originated from adsorbed water. After storing the sample for another three weeks, additional domains became apparent, as higlighted by the green and pink dashed lines in the lateral drive amplitude image in Figure 3i. These domains can only be guessed in the flexural phase image in Figure 3b. This matches our previous observations: We proposed the presence of different PAHs adsorbing on graphitic surfaces under laboratory air conditions.[40,44] We also proposed that the dissipative interaction between the tip and all types of adsorbates was similar in out-of-plane direction, but distinguishable in in-plane direction. The large-scale islands within the area marked by the white dashed lines in Figure 3b were still present. Interestingly, after the first oxygen-plasma treatment of 30 s, the domain structure was still visible in the lateral drive amplitude images of the few-layer graphene/graphite surface. However, the appearance of the domains changed, which is clear when comparing the red with the blue, pink, and green dashed lines in Figure 3j. There are bright circular-shaped domains of around 1–2 μm in size, as indicated by white arrows; there are also relatively dark domains at the upper flake region and close to the flake edge, as marked by the red dotted lines in Figure 3j. Interestingly, only within the areas marked by the blue dashed lines, the lateral drive amplitude remained constant in value, however, at a higher value compared to the image taken before plasma treatment (Figure 3i). In the green and pink marked areas, the lateral drive amplitude partially changes, resulting in new domains (the red dotted lines in Figure 3j). This indicates that adsorbates were partially removed by plasma treatment. Neither the variation in domains, nor the effect of plasma treatment, are visible in the corresponding phase image (Figure 3c); here, the large-scale islands forming from water are still present (white dashed line). After another week of storage, a domain structure similar to that obtained directly after plasma treatment (Figure 3j) was observed on the flake surface in the lateral drive amplitude image, as indicated by the red dashed lines in Figure 3k. Interestingly, stripes with a periodicity of 200–250 nm appeared on a large proportion of the flake, indicated by the yellow dashed lines in Figure 3k. These stripes are also clearly visible in the corresponding phase image in Figure 3d. We observed a similar phenomenon in our recent study,[40] where stripes with a periodicity of ≈50 nm could be detected on graphitic surfaces after heating as well as subsequent storage. The stripes were predominantly aligned along the zigzag direction of the hexagonal carbon lattice. Some of the plasma-induced domains were visible in the flexural phase images, as marked by the white arrows and red dotted lines in Figure 3d. This is an interesting observation because it indicates that the plasma treatment and the re-adsorption within these areas changed the tip-sample out-of-plane dissipative interactions. Consequently, it is reasonable to assume that the material adsorbing during one week's storage is different from the previously present type of adsorbate. Interestingly, the large-scale islands are not visible in Figure 3d (white dashed lines), indicating that the re-adsorbing material covered these islands during the one week of storage. As shown in Figure 3l, after the second plasma treatment of 30 s in the shielded configuration, the overall domain structure remains the same; however, the stripes disappeared and the bright domains (indicated by white arrows) resemble the contrast attributed to water island formation (marked by white dashed lines in the corresponding flexural phase image (Figure 3e)). This was initially surprising because we expected removal of material induced by plasma treatment rather than water island formations. However, this phenomenon has been observed by others and will be discussed in detail in Section 2.4. Plasma-induced water island formation also explains the presence of bright and dark domains in the corresponding phase image in Figure 3e, after the second plasma-treatment step. After another week of storage, the bright and dark domains became less distinct in both the flexural phase and the lateral drive amplitude image (see Figure 3f,m). Nevertheless, the islands (marked by the white dashed lines and white arrows in Figure 3f and outside the red dashed marked areas in Figure 3m) were still apparent. This is indicative of coverage by a single type of adsorbate, however, one that posesses pockets of water. Similar observations were made after the next 30 s plasma-treatment step, as shown in Figure 3g,n and after another one week's storage (Figure S4a,c, Supporting Information) and 30 s plasma treatment (Figure S4b,d, Supporting Information), where bright and dark domains were hardly visible. It can be assumed that the adsorbate material was completely removed from the surface, and that subsequent storage for one week was insufficient to form distinct domains. To further understand adsorbate formation and removal, we analyzed the topographic images corresponding to the ones shown in Figure 3. We determined the height of the different areas G1, G2, and G3 relative to the Si/SiO_2-substrate and found that after the first two weeks of storage, both areas G1 and G2 were lower compared to the substrate (for details see Figure S5, Supporting Information). Consequently, we confirmed that larger quantities of adsorbates were deposited on the Si/SiO_2-substrate compared to the few-layer graphene/graphite flake areas. Additionally, larger quantities of adsorbates were removed from the Si/SiO_2-substrate during the 30 s of plasma treatment compared to the graphene/graphite areas. Both effects compli-

Figure 3. Adsorbate formation on a few-layer graphene/graphite flake analyzed by means of a–g) second flexural phase and h–n) lateral drive amplitude after different durations of storage and oxygen-plasma treatment in AMFlex2-OLTor1-FMLat1 AFM mode. $A_{0\ (flex,2)}$ = 675 nm, $A_{flex,2}$ = 600 nm, and $A_{lat,1}$ = 1.766 nm. The few-layer graphene/graphite flake consists of three areas (G1, G2, and G3, as marked by orange dashed lines in (a)) with different numbers of graphene layers, where the layer number increases from G1 to G3. The white arrow within the color bar (h) indicates the direction of lateral oscillation. Dashed lines (blue, green, pink, and red) highlight the shape of the different domains found on the few-layer graphene/graphite flake surface. Large-scale islands are enclosed by white dashed lines in the flexural phase images (a–g). The orange square in (g) marks the area (350 × 350 nm^2) where the high-resolution images shown in Figure 4 were taken. The assumed adsorbate types of the different subdomains are labeled in the legend.

cate the accurate measurement of the number of graphene layers and hindering the determination of the plasma-treatment time needed to remove the adsorbates from the graphitic surfaces. However, using the information in Figures 2 and 3, we propose that large quantities of adsorbates were already removed after 30 s of plasma treatment; and after another 30 s of plasma treatment, the sample was almost completely adsorbate-free, except for areas where water islands grew. This is in agreement with the Raman spectroscopy results (Figure 2) that show that defects were already introduced after a short plasma treatment (30 s) in the shielded configuration. However, solely observing topographic images is insufficient to corroborate this thesis because the complete removal of adsorbates from the Si/SiO_2-surface takes ≈4 times longer than the complete removal from the graphitic flake areas. In order to corroborate the proposed theory, we recorded and thoroughly analyzed high-resolution images of the same few-layer graphene/graphite flake, within the area marked by the orange square in Figure 3g.

2.4. Stripe-Like Adsorbate and Island Formation Successively Removed by Oxygen-Plasma Treatment

In addition to the adsorbates forming different domains, we also expect stripe-like patterns to form on graphitic surfaces upon storage.[29–39] Based on the results of our previous study,[40] we analyzed the effect of plasma treatment on the stripe-like patterns by using the second flexural phase images, as shown in **Figure 4**. The corresponding lateral drive-amplitude images, in which the stripe-like patterns are also visible, are shown in Figure S6 (Supporting Information).

In Figure 4 the evolution of adsorbate structures was analyzed based on the second flexural-phase images recorded at different magnifications in the AMFlex2-OLTor1-FMLat1 AFM mode. Figure 4a,f shows that the stripe-like pattern of adsorbates is already visible after two weeks of storage, marked by the green dashed lines in Figure 4f, however, not that distinct. Almost the whole scan area of 350 × 350 nm^2 was covered with adsorbates, forming a stripe-like pattern after another three weeks of sample storage (Figure 4b,g). The stripe-like pattern consists of domains with three different orientations that have a 60°-symmetry with respect to each other, as highlighted by the green dashed lines in Figure 4g. The 60°-symmetry of the stripe-like pattern domains originates from the 60°-rotational symmetry found in the hexagonal, honeycomb graphene structure.[29] The periodicity of the stripes is ≈5 nm, which is in agreement with our recent work[40] and within the range of 4–6 nm mentioned by others.[29–39] Pálinkás et al.[39] performed scanning tunneling microscopy (STM) measurements at a temperature of 9 K to clarify the origin of this stripe-like pattern. They showed that the pattern is formed by adsorption of linear alkanes with a length of 20–26 carbon atoms aligned along the zigzag direction of the graphene surface. According to Pálinkás et al.,[39] the periodicity of these stripes (5 nm) at room temperature is equal to the length of the linear alkanes. Consequently, the stripes reflect the orientation of the armchair direction of the graphene lattice. However, it was not possible in our AFM measurements to resolve the molecular structure of the stripe-like pattern at room temperature because the alkane molecules are present in the smectic phase.

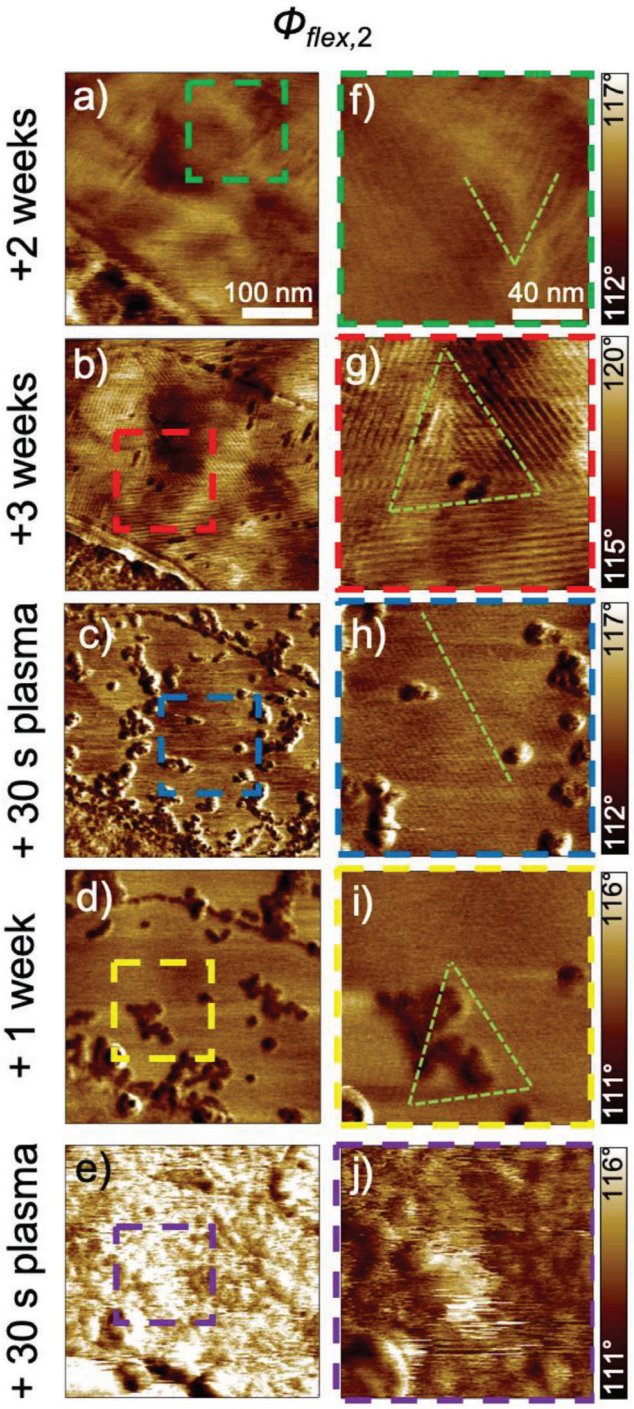

Figure 4. Stripe-like and island structure formation on a few-layer graphene/graphite flake analyzed using the second flexural phase images at two magnifications (a–e) 350 × 350 nm^2 and f–j) 150 × 150 nm^2). Analysis took place after different durations of storage and stepwise oxygen-plasma treatment measured by the AMFlex2-OLTor1-FMLat1 AFM mode. $A_{0\ (flex,2)}$ = 675 nm, $A_{flex,2}$ = 600 nm, and $A_{lat,1}$ = 1.766 nm. The green dashed lines visible in the flexural phase images (f–i) are a guide to the eye to highlight the different orientations of the stripe-like pattern. The dashed squares in (a–e) represent the zoom-in areas for the images shown in (f–j). The same color of these squares represents the same storage or oxygen-plasma treatment step.

After the first 30 s of oxygen-plasma treatment, the stripe-like pattern was still visible on the surface of the investigated flake (Figure 4c,h). In contrast to the acquired phase image taken prior to plasma treatment (Figure 4b,g), the stripe-like pattern was not distinct suggesting that a considerable portion of the adsorbates was removed from the surface of the flake. We conclude that linear alkanes exhibit a sufficiently high binding energy to the graphitic surfaces to at least partly withstand a plasma treatment of 30 s duration in the shielded configuration. To gain a better understanding of the occurrence of the stripe-like pattern before and after the first oxygen-plasma treatment, the corresponding topographic and lateral frequency-shift images were analyzed (Figure S7, Supporting Information). The three stripe-like pattern domains with the aforementioned 60°-symmetry can be seen, as indicated by the green dashed lines in the topographic image in Figure S7a (Supporting Information). In contrast, no stripe-like pattern is visible in the topography image (see Figure S7b, Supporting Information) acquired after 30 s of oxygen-plasma treatment. Comparing the lateral frequency-shift images prior to and after plasma treatment (see Figure S7c,d, Supporting Information) shows that the orientation of the stripe-like pattern changes upon plasma treatment within the same areas (colored polygons); however, some of the stripes remain in their original orientation. The reorientation of the stripe-like pattern was most likely caused by a partial removal of the adsorbates from the graphitic surface due to the first 30 s of plasma treatment. Interestingly, in close proximity to the stripe-like pattern in Figure 4c,h, islands with a diameter between 50 and 100 nm can be observed after the first plasma treatment on the surface of the few-layer graphene/graphite flake. We assume that these islands formed by/during the 30 s of oxygen-plasma treatment, as already implied in Section 2.3. Zhou et al. [45] analyzed the contact angle of water on graphene prior to and after oxygen-plasma treatment. They observed that the oxygen-plasma treatment caused an increase in the hydrophilicity of graphene, and, therefore, a higher tendency for the graphene to adsorb water molecules on its surface. Hence, one potential explanation for the island formation is the adsorption of water molecules on the oxygen-plasma-treated graphene surface. Another possible explanation is that the islands were created by reactive oxygen from the plasma itself, reacting with the graphene surface to form sp^3-type defects. Following the previous discussion on defect evolution upon oxygen-plasma treatment, based on Raman spectroscopy experiments (Section 2.1), sp^3-type defect generation substantiates the interpretation of Zandiatashbar et al. and Lee et al.[26,28] Both groups concluded that prior to reaching a maximum in the intensity ratio between the D-peak and G-peak as a function of plasma-treatment time (transition between stage 1 and stage 2), sp^3-type defects occurred predominantly for graphene samples.

Using scanning probe microscopy techniques, i.e., AFM and STM, Paredes et al.[46,47] investigated the initial stages of oxidation of graphitic surfaces caused by oxygen plasma. The authors observed small protrusions of 1–5 nm in size after a short plasma treatment of 4–6 s with the graphite surface directly facing the plasma source (exposed configuration). These protrusions were not visible in their recorded AFM topographic images, but they were in the lateral force images.[48] Therefore, the authors argued that the occurrence of the protrusions had an electronic origin. They interpreted these protrusions as vacancies formed by oxygen-plasma treatment. Paredes et al.[49] suggested that the friction contrast of the protrusions in lateral force images originated from the occurrence of symmetry-forbidden vibrational lattice modes arising from the symmetry breaking by the formed vacancies. They assigned the contrast visible in the STM images to an increased number of electrons near the Fermi level available for excitation in the vicinity of the vacancies of the graphene lattice. Li et al.[50] also observed these protrusions in their recorded STM images after ozone treatment of HOPG and developed a model to explain the occurrence of the protrusions. Based on the work by Paredes et al.[46] and Li et al.[50] we propose a model for water island formation by oxygen plasma, schematically shown in **Figure 5**. For the processes taking place before water island formation we refer to Figure S9 (Supporting Information).

Li et al.[50] proposed that oxygen from ozone becomes bound in form of epoxy groups at the bridging sites of the graphene lattice, since epoxy groups, compared with other oxygen functional groups (e.g., carbonyl, ether) have a very low defect formation energy. Three oxygen atoms can adsorb at one carbon hexagon to form a cyclic epoxy trimer. The epoxy groups are mobile according to Paredes et al.[46] which means that the cyclic epoxy trimers migrate along the graphene lattice until they meet each other to form a network or cluster. Epoxy groups located in the center of these epoxy clusters change into ether groups, and strain occurs within the center of the cluster. Li et al.[50] suggested that the ether groups escape from the epoxy cluster due to strain build-up, resulting in the release of reaction products, such as carbon monoxide (CO) and carbon dioxide (CO_2). Consequently, vacancies are formed in the center of the epoxy cluster. The epoxy groups together with the vacancies are hydrophilic. Hence, water molecules adsorb on these hydrophilic epoxy clusters and fill the vacancies to form water islands on them.[51]

The white spots between the islands visible in the lateral frequency-shift image in Figure S7d (Supporting Information) are of a similar size (5–10 nm) when comparing with the size of the protrusions reported by Paredes et al.[46] and Li et al.[50] Thus, we propose that the first plasma treatment step in a shielded configuration also creates epoxy clusters with vacancies in their center, and that islands represent water molecule agglomerations on epoxy clusters with vacancies.

Comparing Figure 4d,i with Figure 4c,h shows that the arrangement of the islands changes after one week of storage, possibly either due to diffusion of the islands or manipulation of their position while AFM imaging, as it was reported in our recent work.[40] However, the corresponding 8×8 μm^2 images in Figure 3d,k, in which a large-scale stripe-like arrangement of adsorbates (yellow dashed lines) can be seen, show that this effect is likely caused by a rearrangement of the epoxy clusters/vacancies and their associated water islands along the zigzag direction of the hexagonal lattice. We observed that the small-scale stripe-like pattern was still observable after one week's storage, as indicated by the green dashed lines in Figure 4i. After another plasma treatment step of 30 s, the stripe-like pattern was completely removed from the sample (Figure 4e,j). Surprisingly, the water islands were not completely removed, and the graphitic surfaces appeared perforated. Following the conclusions drawn in Section 2.3, we argue that after 1 min of plasma treatment, the sample was almost completely cleaned from adsorbates, except for some water islands remaining

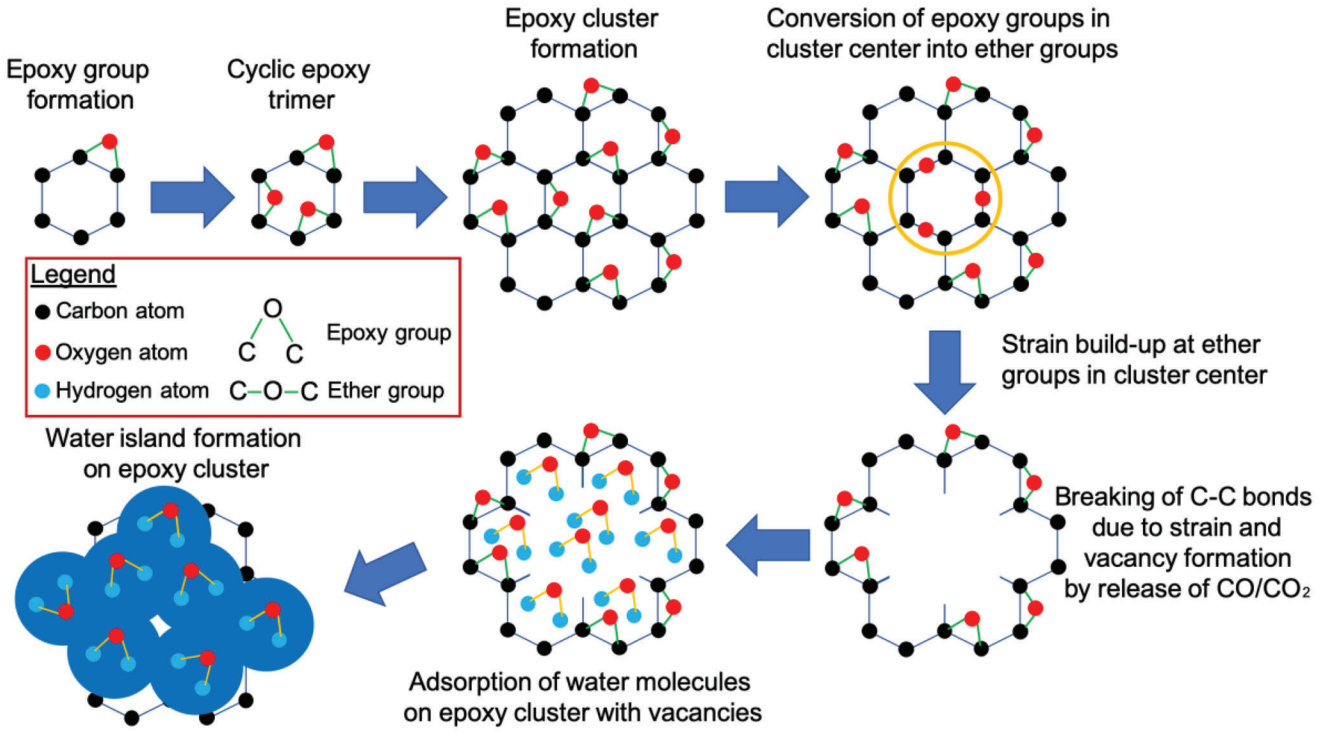

Figure 5. Scheme for oxygen-plasma induced water island formation on graphitic surfaces based on the theories of Paredes et al.[46] and Li et al.[50]

because of the induced epoxy/vacancy clusters. Here we emphasize that despite the fact that the sample was plasma-treated in the shielded configuration, a strongly defective graphene surface was evident after the second plasma-treatment step of 30 s. This must be kept in mind when considering oxygen-plasma treatment as a tool for cleaning graphitic surfaces from adsorbates.

3. Conclusion

We found that airborne adsorbates were present on both Si/SiO_2-substrates and few-layer graphene/graphite flakes. These adsorbates initially prevented the removal of graphene layers from the investigated flakes. Removal of graphene layers occurred after ≈2.5 min of plasma treatment. A further plasma treatment of 16–21 s was required to remove individual layers of graphene (3.0–3.5 layers per min). However, this etching rate for one graphene layer is not straightforwardly transferable to other plasma etching techniques because there are several parameters that can effect the graphene layer ablation and defect generation. The gas type of the plasma treatment, discharge power, treatment time, distance from the powered electrode, and configuration, meaning direct or shielded exposure, have to be considered as well. Using Raman spectroscopy, we showed that defects had been already introduced after ≈30 s of plasma treatment of the graphitic material. From an energetic perspective and based on the analysis of the D/G and D/D' peak ratios, the creation of sp^3-type defects was more likely to occur for shorter plasma-treatment times, whereas the creation of vacancy-type defects was more likely to occur for longer ones.[26] We performed stepwise oxygen-plasma treatment of 30 s duration and subsequent storage for one week to establish a method for the controlled cleaning of graphitic surfaces. Several types of adsorbates and defects were observed at different length scales. At the microscale, different domains with sizes of about 1–2 µm in diameter originating from different species of adsorbed PAHs.[40] PAHs featured different contrasts in the lateral drive amplitude images associated with differences in energy dissipation between the AFM tip and graphene surface under investigation. Interestingly, the formed domains were differently affected by plasma treatment, indicating that the interaction of the adsorbed PAHs with oxygen-plasma depended on the PAH type. At the nanoscale, islands of ≈50–100 nm in diameter were observed after the first oxygen-plasma-treatment step. These islands represented agglomerated water molecules because oxygen-plasma treatment induced the formation of oxygen functional groups; these groups increased the hydrophilicity of the graphene surface. This reflected the evolution of sp^3-type defects after short-period oxygen-plasma treatment. Additionally, stripe-like patterns, with a periodicity of ≈5 nm, were observed in three different orientations with 60° symmetry. These patterns were formed by the adsorption of linear alkanes, consisting of 20–26 carbon atoms.[39] Interestingly, the orientation of some of these stripes changed by 60° upon plasma treatment, indicating the presence of different layers of stripe-like adsorbates stacked on each other.

In summary, the results in this study encourage us to unambiguously identify the types of adsorbates on graphitic samples. Thus we aim to artificially deposit adsorbates in a controlled manner on the surfaces of graphitic materials and subsequently perform Raman spectroscopy and multifrequency AFM. Furthermore, we believe that our method of adsorbate identification can also be applied to other 2D materials with hexagonal lattice

structure such as hexagonal boron nitride (hBN) or molybdenum disulfide (MoS_2) as shown by Pálinkás et al.[39]

4. Experimental Section

HOPG Sample Preparation: HOPG samples were prepared by cleaving both sides using sticky tape. The advantage of double-sided freshly cleaved HOPG samples represents the analysis of the exposed and the shielded area of the sample that result from one and the same plasma treatment process. This facilitates a direct comparison of both treatment options, as shown in Figure S1 (Supporting Information). Furthermore, the Raman spectrum of plasma-treated HOPG is predominantly influenced by the introduced defects. Due to the relatively large HOPG sample thickness, there should be a negligible effect from the number of graphene layers beneath the topmost on the etching rate.

Few-Layer Graphene/Graphite Sample Preparation: The few-layer graphene/graphite samples were prepared via micromechanical exfoliation, following the protocol of Huang et al.[47] The peculiarity of the approach lies in the supplemental heating step when the graphite-flake-decorated tape is in contact with the Si/SiO_2-substrate. Consequently, gases present between the graphite flakes and the substrate evaporate easier than they would without heating; and the probability of synthesizing laterally larger and vertically thinner flakes is increased. The investigated few-layer graphene/graphite sample was stored in a polypropylene storage box under laboratory air conditions. The relative humidity was in the range of 11–57% and the temperature between 12 and 23 °C (see Figure S10, Supporting Information for details). The average relative humidity was 34.25 ± 11.08% and the average temperature was 20.76 ± 1.44 °C.

Oxygen-Plasma Treatment: A FEMTO plasma device (Diener electronic GmbH + Co. KG, Ebhausen, Germany) was used for performing oxygen-plasma treatment of the graphitic materials in this study. The HOPG and few-layer graphene/graphite samples were positioned before each plasma treatment in the plasma chamber of this device in a shielded configuration, as shown in the inset of Figure 1b. The side of the graphitic samples that was supposed to be treated by a reduced plasma dose was placed downward on two glass slides of ≈1 cm gap and 1 mm distance to the surface of a steel plate. The purpose of using the shielded configuration was to remove precisely individual graphene layers and adsorbates from the graphitic samples. After positioning of the samples, the plasma chamber was evacuated to a pressure of 4 mbar and then flushed with oxygen gas for 1 min before gas discharge was initiated at a power of 55 W. The various steps of sample treatment and the cumulative plasma-treatment times for the samples are summarized in Table 1.

Raman Spectroscopy: A sample was analyzed with a WiTec Raman microscope (Oxford Instruments, Ulm, Germany), equipped with a 532 nm laser at a laser power of 1 mW. Image-scans of the few-layer graphene/graphite flake were performed with a pixel size of $\approx 250 \times 250$ nm^2 and an integration time of 0.8 s. The peak intensity ratios were determined by averaging the extracted spectra that can be attributed to one of the areas marked with A, B, C, and D in Figure 1a. Owing to the differences in size of the examined areas, the averaged Raman spectra were determined using 36 spectra for A, 16 spectra for B, nine spectra for C, and two spectra for D. The peak intensities and error bars were determined by Lorentz fitting of the averaged spectra using Igor Pro v6.36 software (WaveMetrics Inc., Lake Oswego, OR, USA).

Atomic Force Microscopy: Two different atomic force microscopes were used for the experiments presented in this work. The topography measurements shown in Figure 1a were performed using a Dimension Icon (Bruker AXS, Santa Barbara, CA) in standard amplitude modulation mode ($A_{flex,1}/A_{0(flex,1)} \approx$ 50–75%) using cantilevers of the type HQ:NSC18/Cr-Au ($k_{flex,1} \approx 2.8$ N m^{-1}, $f_{flex,1} \approx 76$ kHz). Multifrequency AFM measurements were performed using a Cypher S atomic force microscope (Asylum Research, Oxford Instruments, Santa Barbara, CA). The instrument was equipped with a blueDrive photothermal excitation setup, allowing for simultaneous in-plane and out-of-plane excitation of the cantilever if the power-modulated laser is focused at the fixed end of the cantilever, however, some micrometers off the length symmetry axis. Details of the setup for performing the AMFlex2-OLTor1-FMLat1-FMFlex3 AFM method can be found in the recent publications.[40,41,52] Here cantilevers of the type HiRes-C15/Cr-Au purchased from Mikromasch (Innovative Solutions Bulgaria Ltd., Sofia, Bulgaria) were used.

Supporting Information

Supporting Information is available from the Wiley Online Library or from the author.

Acknowledgements

A.L.E. and M.H. contributed equally to this work. The authors thank Alena Bell for supporting them with analysis of the Raman measurements and the Deutsche Forschungsgemeinschaft (Project number 407750697) for financial support.

Open access funding enabled and organized by Projekt DEAL.

Conflict of Interest

The authors declare no conflict of interest.

Data Availability Statement

The data that support the findings of this study are available from the corresponding author upon reasonable request.

Keywords

adsorbates, graphene, in-plane and out-of-plane mechanical properties, multifrequency atomic force microscopy, plasma treatment

Received: March 29, 2023
Revised: May 27, 2023
Published online: July 2, 2023

[1] K. S. Novoselov, A. K. Geim, S. V. Morozov, D. Jiang, Y. Zhang, S. V. Dubonos, I. V. Grigorieva, A. A. Firsov, *Science* **2004**, *306*, 666.
[2] Li Sun, W. Kong, Y. Jiang, H. Wu, K. Jiang, J. Wang, S. Fan, *J. Mater. Chem. A* **2015**, *3*, 5305.
[3] Y. Song, A. Osherov, V. Bulović, J. Kong, *Adv. Sustainable Syst.* **2018**, *2*, 1700106.
[4] L. Bai, Y. Zhang, W. Tong, Li Sun, H. Huang, Qi An, Na Tian, P. K. Chu, *Electrochem. Energy Rev.* **2019**, *3*, 395.
[5] N. Natter, N. Natter, N. Kostoglou, C. Koczwara, C. Tampaxis, T. Steriotis, R. Gupta, O. Paris, C. Rebholz, C. Mitterer, *C* **2019**, *5*, 16.
[6] E. Mccann, V. I. Fal'ko, *Phys. Rev. Lett.* **2006**, *96*, 086805.
[7] E. Suárez Morell, M. Pacheco, L. Chico, L. Brey, *Phys. Rev. B* **2013**, *87*, 125414.
[8] Li-F Sun, Li-M Dong, Z.-F. Wu, C. Fang, *Chin. Phys. B* **2013**, *22*, 077201.
[9] N. Ferralis, *J. Mater. Sci.* **2010**, *45*, 5135.
[10] C. Thomsen, S. Reich, *Phys. Rev. Lett.* **2000**, *85*, 5214.
[11] A. C. Ferrari, *Solid State Commun.* **2007**, *143*, 47.
[12] R. J. Nemanich, S. A. Solin, *Phys. Rev. B* **1979**, *20*, 392.
[13] A. C. Ferrari, J. C. Meyer, V. Scardaci, C. Casiraghi, M. Lazzeri, F. Mauri, S. Piscanec, D. Jiang, K. S. Novoselov, S. Roth, A. K. Geim, *Phys. Rev. Lett.* **2006**, 97.

[14] I.-Y. Jeon, Y.-R. Shin, G.-J. Sohn, H.-J. Choi, S.-Y. Bae, J. Mahmood, S.-M. Jung, J.-M. Seo, M.-J. Kim, D. Wook Chang, L. Dai, J.-B. Baek, *Proc. Natl. Acad. Sci. U. S. A.* **2012**, *109*, 5588.
[15] W. Zhao, M. Fang, F. Wu, H. Wu, L. Wang, G. Chen, *J. Mater. Chem.* **2010**, *20*, 5817.
[16] Y. Hernandez, V. Nicolosi, M. Lotya, F. M. Blighe, Z. Sun, S. De, I. T. Mcgovern, B. Holland, M. Byrne, Y. K. Gun'ko, J. J. Boland, P. Niraj, G. Duesberg, S. Krishnamurthy, R. Goodhue, J. Hutchison, V. Scardaci, A. C. Ferrari, J. N. Coleman, *Nat. Nanotechnol.* **2008**, *3*, 563.
[17] P. R. Somani, S. P. Somani, M. Umeno, *Chem. Phys. Lett.* **2006**, *430*, 56.
[18] K. S. Hazra, J. Rafiee, M. A. Rafiee, A. Mathur, S. S. Roy, J. Mclauhglin, N. Koratkar, D. S. Misra, *Nanotechnology* **2010**, *22*, 025704.
[19] G. Zhao, D. Shao, C. Chen, X. Wang, *Appl. Phys. Lett.* **2011**, *98*, 183114.
[20] C.-M. Seah, B. Vigolo, S.-P. Chai, A. R. Mohamed, *Carbon* **2016**, *105*, 496.
[21] H. Al-Mumen, F. Rao, W. Li, L. Dong, *Nano-Micro Lett.* **2014**, *6*, 116.
[22] D. C. Kim, D.-Y. Jeon, H.-J. Chung, Y. Woo, J. K. Shin, S. Seo, *Nanotechnology* **2009**, *20*, 375703.
[23] H. Mao, R. Wang, J. Zhong, S. Zhong, W. Chen, *Carbon* **2014**, *76*, 212.
[24] I. Childres, L. A. Jauregui, J. Tian, Y. P. Chen, *New J. Phys.* **2011**, *13*, 025008.
[25] A. Eckmann, A. Felten, A. Mishchenko, L. Britnell, R. Krupke, K. S. Novoselov, C. Casiraghi, *Nano Lett.* **2012**, *12*, 3925.
[26] G. Lee, J. Kim, K. Kim, J. W. Han, *J. Vac. Sci. Technol., A* **2015**, *33*, 060602.
[27] A. C. Ferrari, J. Robertson, *Phys. Rev. B* **2001**, *64*, 075414.
[28] A. Zandiatashbar, G.-H. Lee, S. J. An, S. Lee, N. Mathew, M. Terrones, T. Hayashi, C. R. Picu, J. Hone, N. Koratkar, *Nat. Commun.* **2014**, *5*, 3186.
[29] P. Gallagher, M. Lee, F. Amet, P. Maksymovych, J. Wang, S. Wang, X. Lu, G. Zhang, K. Watanabe, T. Taniguchi, D. Goldhaber-Gordon, *Nat. Commun.* **2016**, *7*, 10745.
[30] P. Gallagher, Y. Li, K. Watanabe, T. Taniguchi, T. F. Heinz, D. Goldhaber-Gordon, *Nano Lett.* **2018**, *18*, 2603.
[31] D. S. Wastl, F. Speck, E. Wutscher, M. Ostler, T. Seyller, F. J. Giessibl, *ACS Nano* **2013**, *7*, 10032.
[32] D. Zhang, Y. Zhang, Q. Li, M. Dong, *Friction* **2022**, *10*, 573.
[33] A. Temiryazev, A. Frolov, M. Temiryazeva, *Carbon* **2019**, *143*, 30.
[34] Y.-H Lu, C.-W. Yang, I.-S. Hwang, *Langmuir* **2012**, *28*, 12691.
[35] Y.-H Lu, C.-W. Yang, C.-K. Fang, H.-C. Ko, I.-S. Hwang, *Sci. Rep.* **2014**, *4*, 7189.
[36] N. Haghighian, D. Convertino, V. Miseikis, F. Bisio, A. Morgante, C. Coletti, M. Canepa, O. Cavalleri, *Phys. Chem. Chem. Phys.* **2018**, *20*, 13322.
[37] M. V. Rastei, B. Heinrich, J. L. Gallani, *Phys. Rev. Lett.* **2013**, *111*, 084301.
[38] S. Seibert, S. Klassen, A. Latus, R. Bechstein, A. Kühnle, *Langmuir* **2020**, *36*, 7789.
[39] A. Pálinkás, G. Kálvin, P. Vancsó, K. Kandrai, M. Szendrő, G. Németh, M. Németh, Á. Pekker, J. S. Pap, P. Petrik, K. Kamarás, L. Tapasztó, P. Nemes-Incze, *Nat. Commun.* **2022**, *13*, 6770.
[40] A. L. Eichhorn, M. Hoffer, C. Dietz, *Carbon* **2022**, *200*, 124.
[41] A. L. Eichhorn, C. Dietz, *Sci. Rep.* **2022**, *12*, 8981.
[42] L. Xie, L. Jiao, H. Dai, *J. Am. Chem. Soc.* **2010**, *132*, 14751.
[43] E. H. M. Ferreira, M. V. O. Moutinho, F. Stavale, M. M. Lucchese, R. B. Capaz, C. A. Achete, A. Jorio, *Phys. Rev. B* **2010**, *82*, 125429.
[44] B. Li, P. Ou, Y. Wei, X. Zhang, J. Song, *Materials* **2018**, *11*, 726.
[45] H. Zhou, A. Uysal, D. M. Anjos, Y. Cai, S. H. Overbury, M. Neurock, J. K. Mcdonough, Y. Gogotsi, P. Fenter, *Adv. Mater. Interfaces* **2015**, *2*, 1500277.
[46] J. I. Paredes, A. Martínez-Alonso, J. M. D. Tascón, *Langmuir* **2002**, *18*, 4314.
[47] J. I. Paredes, A. Martínez-Alonso, J. M. D. Tascón, *Langmuir* **2007**, *23*, 8932.
[48] P. Solís-Fernández, J. I. Paredes, M. J. López, I. Cabria, J. A. Alonso, A. Martínez-Alonso, J. M. D. Tascón, *J. Phys. Chem. C* **2009**, *113*, 18719.
[49] J. I. Paredes, A. Martinez-Alonso, J. M. D. Tascon, *J. Microsc. (Oxford, U. K.)* **2003**, *210*, 119.
[50] S. Li, M. T. Vahdat, S. Huang, K.-J. Hsu, M. Rezaei, M. Mensi, N. Marzari, K. V. Agrawal, *JACS Au* **2022**, *2*, 723.
[51] C. L. Mccallum, T. J. Bandosz, S. C. Mcgrother, E. A. Müller, K. E. Gubbins, *Langmuir* **1999**, *15*, 533.
[52] A. L. Eichhorn, C. Dietz, *Adv. Mater. Interfaces* **2021**, *8*, 2101288.